

Article

Phonon Structure, Infra-Red and Raman Spectra of Li_2MnO_3 by First-Principles Calculations

Ruth Pulido ^{1,2}, Nelson Naveas ^{1,2,*}, Raúl J. Martín-Palma ¹, Fernando Agulló-Rueda ³,
Victor R. Ferró ⁴, Jacobo Hernández-Montelongo ^{5,*}, Gonzalo Recio-Sánchez ⁶, Ivan Brito ⁷
and Miguel Manso-Silván ^{1,8}

- ¹ Departamento de Física Aplicada and Instituto Universitario de Ciencia de Materiales Nicolás Cabrera, Universidad Autónoma de Madrid, 28049 Madrid, Spain
- ² Departamento de Ingeniería Química y Procesos de Minerales, Universidad de Antofagasta, Avenida Angamos 601, Antofagasta 1240000, Chile
- ³ Instituto de Ciencia de Materiales de Madrid (ICMM), CSIC, 28049 Madrid, Spain
- ⁴ Departamento de Ingeniería Química, Universidad Autónoma de Madrid, 28049 Madrid, Spain
- ⁵ Departamento de Ciencias Matemáticas y Físicas, UC Temuco, Temuco 4813302, Chile
- ⁶ Facultad de Ingeniería, Arquitectura y Diseño, Universidad de San Sebastián, Concepción 4080871, Chile
- ⁷ Departamento de Química, Universidad de Antofagasta, Avenida Angamos 601, Antofagasta 1240000, Chile
- ⁸ Centro de Microanálisis de Materiales, Universidad Autónoma de Madrid, Campus de Cantoblanco, 28049 Madrid, Spain
- * Correspondence: nelson.naveas@estudiante.uam.es (N.N.); jacob.hernandez@uct.cl (J.H.-M.); Tel.: +34-914974919 (N.N.); +56-452205289 (J.H.-M.)



Citation: Pulido, R.; Naveas, N.; Martín-Palma, R.J.; Agulló-Rueda, F.; Ferró, V.R.; Hernández-Montelongo, J.; Recio-Sánchez, G.; Brito, I.; Manso-Silván, M. Phonon Structure, Infra-Red and Raman Spectra of Li_2MnO_3 by First-Principles Calculations. *Materials* **2022**, *15*, 6237. <https://doi.org/10.3390/ma15186237>

Academic Editor: Aleksandr Oreshonkov

Received: 15 August 2022

Accepted: 2 September 2022

Published: 8 September 2022

Publisher's Note: MDPI stays neutral with regard to jurisdictional claims in published maps and institutional affiliations.



Copyright: © 2022 by the authors. Licensee MDPI, Basel, Switzerland. This article is an open access article distributed under the terms and conditions of the Creative Commons Attribution (CC BY) license (<https://creativecommons.org/licenses/by/4.0/>).

Abstract: The layer-structured monoclinic Li_2MnO_3 is a key material, mainly due to its role in Li-ion batteries and as a precursor for adsorbent used in lithium recovery from aqueous solutions. In the present work, we used first-principles calculations based on density functional theory (DFT) to study the crystal structure, optical phonon frequencies, infra-red (IR), and Raman active modes and compared the results with experimental data. First, Li_2MnO_3 powder was synthesized by the hydrothermal method and successively characterized by XRD, TEM, FTIR, and Raman spectroscopy. Secondly, by using Local Density Approximation (LDA), we carried out a DFT study of the crystal structure and electronic properties of Li_2MnO_3 . Finally, we calculated the vibrational properties using Density Functional Perturbation Theory (DFPT). Our results show that simulated IR and Raman spectra agree well with the observed phonon structure. Additionally, the IR and Raman theoretical spectra show similar features compared to the experimental ones. This research is useful in investigations involving the physicochemical characterization of Li_2MnO_3 material.

Keywords: Li_2MnO_3 ; DFT; DFPT; Raman spectroscopy; IR spectroscopy

1. Introduction

The growing demand for portable devices, electronic vehicles and energy storage, as well as attempts to mitigate the impacts of global warming, have led to rapid advances in the development of lithium-ion batteries as well as the search for new technologies in lithium recovery [1–4]. In this instance, lithium manganese oxide (LMO) materials have attracted a great deal of interest due to their key roles as cathodic and precursor materials for energy and lithium adsorption from aqueous solutions, respectively [5,6]. In the context of these potential applications, Li-rich LMO such as Li_2MnO_3 has been identified as a crucial component due to its interesting physicochemical properties [7,8]. Interestingly, it has been reported that the increase of Li_2MnO_3 content enhances the cycling stability of cathode materials based on Li-Mn-O, preventing the manganese dissolution [9,10]. Similarly, by controlling the Li_2MnO_3 layered phase content in lithium adsorbent precursor materials, it is possible to prevent the manganese dissolution from the LMO lattice during the Li^+ desorption process [11].

The layer-structured monoclinic Li_2MnO_3 materials (with the rock salt crystal structure; Figure 1) belong to the $C2/m$ space group. Li_2MnO_3 structure consists of laminations of alternating Li/Mn and Li-layers (Figure 1a). The Li^+ and Mn^{+4} ions reside in the octahedral interstices of a close-packed cubic oxygen lattice stacking order, as represented in Figure 1b,c [12]. Their formula can also be written as:

$$\{(Li_{1/2})_{2c}(Li_1)_{4h}\}_{interslab}\{(Li_{1/2})_{2b}(Mn_1)_{4g}(O_1)_{4i}(O_2)_{8j}\}$$

The lithium ions are scattered octahedrally in the 2c and 4h Wyckoff position inside the $[\text{Li}^+]$ layer and in the 2b position into the $[\text{LiMn}_2]$ layer, while the Mn^{+4} ions are dispersed octahedrally in the 4g sites [13].

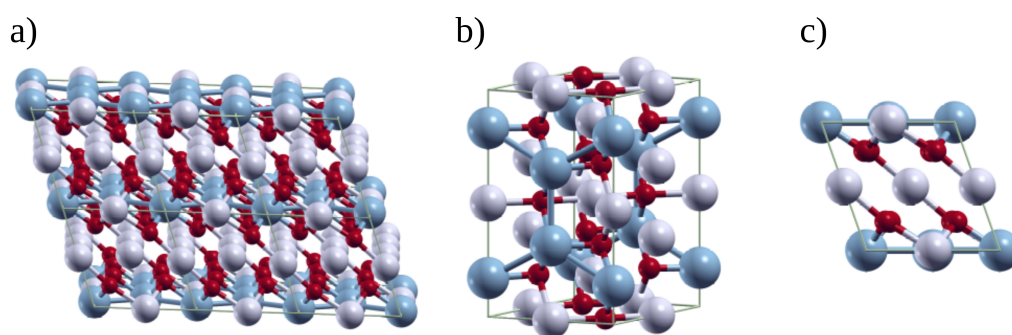


Figure 1. (a) A $2 \times 1 \times 2$ super-cell showing the $[\text{Li}^+]$ and $[\text{LiMn}_2]$ layers, (b) the conventional unit cell, and (c) the top view of the monoclinic Li_2MnO_3 crystal (Li: grey, Mn: blue and O: red).

Li_2MnO_3 -based LMO materials can be formed by different synthesis routes, varying in conformation and composition. Structures such as core-shell type, spinel embedded within the layered matrix, and spherical particles have been reported [9,14,15]. Whatever the conformation and composition are chosen, a detailed characterization of the LMO material is essential to provide an understanding of its different properties. For example, one of the most critical issues in understanding electrochemical properties is determining the local structure [16]. In this context, some studies have shown a relationship between the structural properties and electrochemical performance in doped-LMO composites [7,17]. Kim et al. reported that the enhanced stability of the local structure of lithium manganese oxides is related to the improvement of cyclability [18]. Likewise, the knowledge of the local environment of LMO helps to elucidate the underlying mechanism of the ad/desorption process in LMO-based lithium-ion sieves [19]. In this sense, vibrational spectroscopy can be used to provide information on the structural aspects of LMO. Raman and infra-red (IR) spectroscopies are very sensitive to the short-range environment of oxygen coordination around the cations [20]. Julien and co-workers have extensively studied the structural properties of spinel-type LMO by Raman and IR spectroscopies [20–26]. Their results are based on the experimental analysis of the LMO building blocks, namely, the tetrahedra LiO_4 and the octahedra MnO_6 , which compose the crystal lattice. On the contrary, the vibrational analysis of the Li_2MnO_3 has not been completely and vigorously studied yet, despite the fact that its IR and/or Raman bands have been studied previously by experiments [8,27]. Therefore, there is a need to perform detailed studies in order to obtain solid knowledge about its vibrational properties. In this context, simulated IR and Raman spectra based on density functional theory (DFT) calculations can be helpful in understanding the vibrational properties of Li_2MnO_3 . In fact, DFT-based theoretical studies have shown excellent agreement with experimental IR and/or Raman spectra of organic compounds [28], crystalline [29], and 2D materials [30].

In the present work, we report a computational study of the vibrational properties of Li_2MnO_3 . Initially, we synthesized and physicochemically characterized the Li_2MnO_3 powder material. Further, we proceeded to the calculation of the optimized crystal structure and the electronic properties by first-principle calculations using the Local Density

Approximation (LDA). Then, by using Density Functional Perturbation Theory (DFPT), we studied the vibrational modes and computed the phonon structure, IR and Raman spectra of the Li_2MnO_3 . Finally, a detailed interpretation of obtained data was presented.

2. Materials and Methods

2.1. Material Synthesis and Characterization

The Li_2MnO_3 samples were synthesized by way of a hydrothermal method. First, LiOH ($2 \text{ mol}\cdot\text{L}^{-1}$) and H_2O_2 ($1.2 \text{ mol}\cdot\text{L}^{-1}$) were dissolved in ultra-pure water to produce Li precursor solutions. Then, MnSO_4 ($0.4 \text{ mol}\cdot\text{L}^{-1}$) was dissolved in ultra-pure water to form an Mn precursor solution. Both solutions were magnetically stirred for 2 h. Subsequently, the mixture was crystallized for 8 h at 180°C in a Teflon-lined stainless steel autoclave. The crystallization product was washed and centrifuged numerous times. Finally, the resultant product was dried at 60°C for 12 h before being calcined at 800°C for 4 h.

Powder X-ray Diffraction (XRD) in a Bruker New D8 Advance X-ray diffractometer equipped with a Johansson monochromator (Cu-K α 1 radiation (Billerica, MA, USA), $\lambda = 1.5406 \text{ \AA}$) and LYNXEYE XE detector was used to investigate the Li_2MnO_3 crystallographic structure. With an angular step of 0.02° and a scanning rate of $2^\circ/\text{s}$, the diffraction patterns were scanned from 2θ 10° to 90° .

High-resolution transmission electron microscopy (HR-TEM) and electron diffraction (ED) (JEOL 2100F, Tokyo, Japan), operating under an accelerating voltage of 200 kV, were used to analyze the morphology and microstructure of Li_2MnO_3 samples.

The vibrational properties of Li_2MnO_3 samples were studied by Raman, and Fourier transform infrared (FT-IR) spectroscopies. Raman spectra were acquired from Renishaw Ramascope 2000 Raman microspectrometer, coupled to an Olympus BH-2 optical microscope at room temperature using argon ion laser (514.5 nm wavelength (green)) for excitation. The objective had a numerical aperture of $\text{NA} = 0.80$ and a magnification of $50\times$. On the sample surface, the laser power was of the order of 1 mW. Each CCD pixel integration time was 50 s. The FT-IR spectra were obtained from Spectrum Two Spectrometer (Perkin Elmer; Waltham, MA, USA) with a resolution of 4 cm^{-1} over the range of $4000\text{--}50 \text{ cm}^{-1}$.

2.2. Calculation Details

The calculations were carried out under the Density Functional Theory (DFT) framework using the plane wave pseudopotential method coded inside the Quantum ESPRESSO computational package [31]. We used the conventional unit cell to represent Li_2MnO_3 , which is composed of four formula units, resulting in a total of 24 atoms ($\text{Li}_8\text{Mn}_4\text{O}_{12}$; see Figure 1b). Then, the optimized cell parameters were obtained via DFT by variable-cell relaxation. For Li, Mn, and O atoms, norm-conserving pseudopotentials based on Local Density Approximation (LDA) were selected [32]. We used very tight values for the kinetic energy cutoff, total energy and force tolerance, setting them to 80 Ry, 1×10^{-9} Ry and 1×10^{-5} Ry per Bohr, respectively. In order to sample the reciprocal space, we used the Monkhorst–Pack method [33] with a k-point mesh of $4 \times 4 \times 4$ for the cell model, $\text{Li}_8\text{Mn}_4\text{O}_{12}$. Despite the fact that the nature of Li_2MnO_3 is antiferromagnetic, several reports demonstrated that the effect of various spin configurations on the total formation energies is minimal; therefore, in order to simplify the model, only the ferromagnetic configuration is taken into account when the spin polarization is included in the calculations [13,34–36]. The optimized cell parameters and atomic positions were used to construct the electronic density of states (DOS) and the electronic band structure. In order to calculate the vibrational properties, we performed Density Functional Perturbation Theory (DFPT) using the Phonon Package of Quantum ESPRESSO [37]. Using the DFPT linear response approach at the Γ point, the dynamic matrix and frequencies of the harmonic phonon modes were determined. The calculated IR and Raman spectra were represented by a Gaussian function with an FWHM of 10 cm^{-1} . The vibrational modes were visualized with the XCrysDen software [38]. The phonon band structure and phonon DOS were computed by using a q-point mesh of $2 \times 2 \times 2$.

3. Results and Discussion

3.1. Characterization of the Li_2MnO_3 Powder Material

The performance of the LMO is strongly influenced by the crystalline structure, particle size, morphology and specific surface area. Therefore, it is important to conduct a detailed characterization before its application [11]. In order to characterize synthesized Li_2MnO_3 in terms of crystalline structure, we performed XRD analysis (Figure 2a). The high sharpness and intensity of the experimental peaks are remarkable indicators of the good crystalline nature of the material. Characteristic peaks of monoclinic Li_2MnO_3 ($C2/m$ spatial group; COD entry # 96-154-4474) [39] can be distinguished. Thus, between 20° and 25° , shoulder-like peaks related to the diffraction of the superlattice of Li_2MnO_3 are observed [40]. Moreover, the samples display the typical peak splitting between $63\text{--}67^\circ$, corresponding to the (-133) and $(33-1)$ planes.

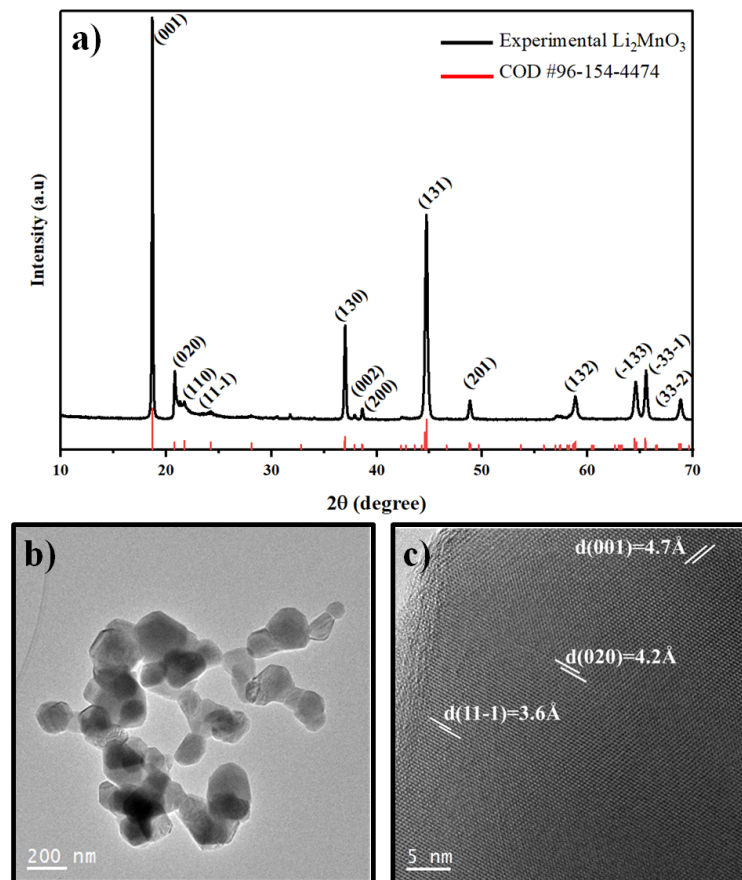


Figure 2. (a) X-ray diffraction pattern and (b,c) Transmission Electron Microscopy images of the Li_2MnO_3 powder material used in this study.

HRTEM was used for the local study of the microstructure of LMO. HRTEM images (Figure 2b) show the presence of agglomerated nanoparticles with granular morphology and particle sizes between 100 and 200 nm. Moreover, by analyzing the HRTEM image in Figure 2c, it is possible to identify the $[001]$, $[020]$ and $[11-1]$ zone axes with interplanar spacings of 4.7 Å, 4.2 Å and 3.6 Å, respectively, which correspond to the layered structure Li_2MnO_3 [11,41].

3.2. Optimized Crystal Structure and Electronic Properties of the Li_2MnO_3

The Li_2MnO_3 crystal structure exhibits a monoclinic spatial ordering with a space group $C2/m$. The parameters of the conventional unit cell are $a = 4.933$ Å, $b = 8.535$ Å, $c = 5.026$ Å and $\beta = 109.314^\circ$ [42,43]. Herein, the Mn^{+4} ions are arranged in octahedral 4g sites, while the lithium-ion, Li^+ , are spread in 2c and 4h octahedral sites into the $[\text{LiMn}_2]$

layer and $[Li^+]$ layer stack [3]. Thus, we first calculated the structural parameters of the relaxed conventional unit cell of the Li_2MnO_3 by using the LDA method and compared them to the experimental values (Table 1). On the one hand, the results showed that the calculated lattice parameters a , b and c were underestimated by the LDA method compared to the experimental values by approximately 3%. On the contrary, the β angle (the angle between axes a and c) was slightly overestimated. Despite the fact that LDA has been shown to underestimate the lattice parameters for several types of materials severely, our optimized lattice parameters for the Li_2MnO_3 present good agreement with the experimental results.

Table 1. Optimized structural parameters of the Li_2MnO_3 crystal determined by DFT calculations.

	a (Å)	b (Å)	c (Å)	β (°)	Volume (Å ³)
LDA	4.805	8.308	4.854	109.628	182.494
Experimental	4.933	8.535	5.026	109.314	211.608

Figure 3 shows the predicted projected density of states (pDOS) and band structure of the Li_2MnO_3 along with the high-symmetry points of the first Brillouin zone. The Fermi energy level (E_F) has been set to zero energy. The electronic DOS of the Figure 3 shows an overlap/hybridization between the $3d$ state of Mn and the $2p$ state of O, which is characteristic of $3d$ transition metal oxides [35]. The occupied states at the Fermi level are largely constituted of O $2p$, while the Mn $3d$ orbitals contribute more to the conduction bands. The band gap between the lowest conduction and maximum valence levels are 1.65 eV and 1.99 eV for the spin-up and down configuration, respectively, thus assuming a semiconductor behavior. On the other hand, the electronic band structure of Li_2MnO_3 indicates that both valence band maximum and conduction band minimum are localized at the Γ -point.

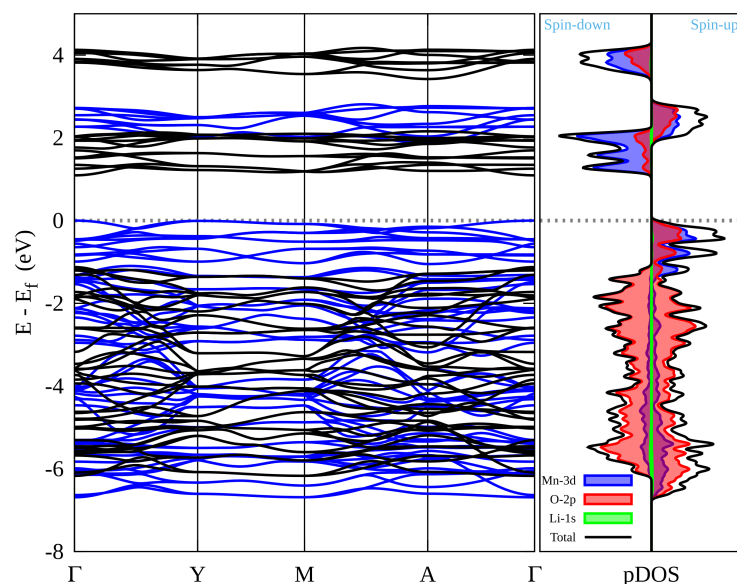


Figure 3. Electronic band structure and electronic density of states of Li_2MnO_3 calculated by LDA. In the electronic band structure, the blue and black bands correspond to the spin-up and down, respectively.

3.3. Vibrational Properties of Li_2MnO_3

The computed phonon bands dispersion and phonon DOS for Li_2MnO_3 along the high-symmetry directions of the first Brillouin zone are shown in Figure 4. Importantly, the absence of imaginary frequency modes in the Brillouin zone demonstrates the structural

dynamical stability of our model of Li_2MnO_3 [44,45]. According to the dispersion curves in Figure 4, the highest wavenumber is about 700 cm^{-1} . More interestingly, the phonon band structure of Li_2MnO_3 does not contain a phonon gap [45]. The phonon DOS for Li_2MnO_3 is shown on the right-hand of Figure 4. The shaded green, red, and blue areas represent Li, O, and Mn atom phonon partial DOS, respectively. On the one hand, it is evident that the O atom contributes to the overall phonon distribution, dominating the zone with the highest intensities at higher frequencies. Additionally, the phonon distribution of the Mn atom extends to the whole spectrum but with lower intensity than the O atom. Interestingly, there is a hybridization between Mn and O vibrational states at higher frequencies. On the other hand, the phonon distribution of the Li atom mainly contributes to the middle part of the spectrum, ranging from 200 cm^{-1} to 500 cm^{-1} , suggesting hybridization between Li and O vibrational states in this zone.

The unit cell of Li_2MnO_3 has 24 atoms. After the software analysis, there are three acoustic and sixty-nine optical modes. Li_2MnO_3 belongs to the C_{2h} space group (point group C_{2h}), and its irreducible representations at the Brillouin zone point are the following:

$$\Gamma_{acoustic} = A_u + 2B_u \quad (1)$$

$$\Gamma_{optic} = 15A_u + 12A_g + 24B_u + 16B_g. \quad (2)$$

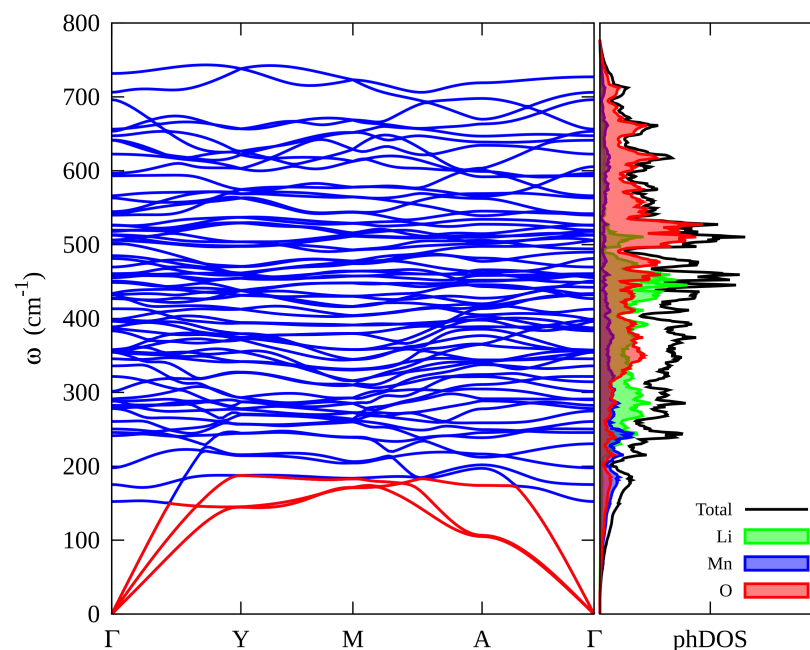


Figure 4. Phonon dispersion and phonon DOS for Li_2MnO_3 calculated by using the LDA method. In the phonon band structure, the acoustic bands are plotted in red.

Tables 2 and 3 show the calculated Γ zone-centered optical phonon frequencies of Li_2MnO_3 . In Li_2MnO_3 , according to the C_{2h} point group character table, the A_u and B_u modes are IR active, whereas the A_g and B_g modes are Raman active. The lowest and highest phonon frequencies are 173.38 and 668.64 cm^{-1} , respectively, which is consistent with our previous results of the computed phonon dispersion.

Table 2. Experimental and calculated IR modes for the Li₂MnO₃ crystal determined by DFPT calculations.

Exp. IR freq.(cm ⁻¹)	Calc. IR freq.(cm ⁻¹)	Symmetry	Exp. IR freq.(cm ⁻¹)	Calc. IR freq.(cm ⁻¹)	Symmetry
	173.38	B _u		417.7	B _u
	181.89	A _u	425	431.79	A _u
	184.75	B _u		439.87	B _u
	208.99	B _u	437.8	461.78	A _u
	226.19	B _u	437.8	469.48	B _u
	252.46	A _u		489.38	A _u
	258.53	B _u		498.5	B _u
268	263.69	B _u		501.37	A _u
282	274.87	A _u	514	507.57	B _u
282	276.48	B _u		530.38	B _u
292	306.25	B _u		543.95	B _u
327	316.27	A _u	537	570.37	A _u
	334.01	A _u	537	579.04	B _u
352	350.02	B _u	537	581.66	B _u
352	354.15	B _u	627	609.12	A _u
	367.76	B _u	627	613.16	B _u
380	378.5	B _u	627	622.42	A _u
	393	A _u	627	628.49	A _u
	401.78	A _u	627	633.94	B _u
	407.29	B _u			

Table 3. Experimental and calculated Raman modes for the Li₂MnO₃ crystal determined by DFPT calculations.

Exp. Raman freq.(cm ⁻¹)	Calc. Raman freq.(cm ⁻¹)	Symmetry	Exp. Raman freq.(cm ⁻¹)	Calc. Raman freq.(cm ⁻¹)	Symmetry
	201.07	A _g		482.56	A _g
	218.24	A _g	501	493.99	B _g
	224.08	B _g	501	514.9	B _g
250	238.84	B _g	501	520.66	A _g
309	300.07	B _g	501	522.63	A _g
324	322.81	B _g		549.63	B _g
335	347.34	B _g		552.83	B _g
374	372.87	A _g		565.07	B _g
374	376.47	A _g	574	572.2	B _g
	390.11	A _g	574	574.7	A _g
419	427.5	A _g	616	619.61	A _g
	435.11	B _g		623.26	A _g
442	441.91	B _g		668.64	A _g
	454.22	A _g			

The experimental and theoretical IR and Raman spectra are shown in Figure 5. The IR and Raman spectra calculated for Li₂MnO₃ were based on lattice dynamic simulations. As has been previously shown for other transition metal oxides, in our case, the number of experimental modes is much lower than that expected theoretically due to the three possible circumstances: (i) certain modes have very similar energy; (ii) stronger bands may overlap some weaker bands, and (iii) in spectra of a randomly oriented crystalline material, the relevant bands cannot be resolved properly [46,47].

Figure 5a shows the FT-IR spectra of synthesized Li₂MnO₃ powder. The sample exhibited strong absorption bands around 500–700 cm⁻¹. Specifically, these bands appear at 514, 537 and 627 cm⁻¹. The major contribution of these bands is related to the asymmetric stretching vibrations of octahedral MnO₆ [21,25]. In this range, however, the stretching vibrations of tetrahedral LiO₄ groups have also been observed at 650 cm⁻¹ [19]

and 350–550 cm^{-1} [23]. IR spectroscopy investigations of lithium inorganic compounds have demonstrated that the vibrations of MnO_6 groups are tightly related to LiOn polyhedral vibrational modes at low and high frequencies (LiO_6 and LiO_4) [21]. The calculated IR spectra of Li_2MnO_3 are shown in Figure 5b. Interestingly, the theoretical spectrum shows similar characteristics to the experimental one, with some shifts in the frequency of the main vibrational modes. The results show two IR active modes with high intensity at higher frequencies (550–650 cm^{-1}). Additionally, four intense IR active modes appear at the middle-to-low frequencies zone (250–510 cm^{-1}). The absorption bands around 550–650 cm^{-1} and 250–510 region are attributed mainly to the MnO_6 and LiOn functional groups, respectively, as can be seen in the atomic displacements for the IR vibrations modes of Li_2MnO_3 (Figure 6). Remarkably, these theoretical results are in agreement with the phonon study, which shows a strong hybridization between Li-O and Mn-O at low and high frequencies, respectively.

Figure 5c shows the typical Raman spectra of the synthesized Li_2MnO_3 powder. Eight major contributions are resolved with clarity. Strong bands at high frequencies, related to the stretching of Mn-O bond modes that arise from the MnO_6 octahedra, are evidenced [48]. Additionally, weak bands in the low-frequency region related to Li-O bonds are observed [49]. The Raman spectra exhibited active Raman bands around 616, 574, 501, 442, 419, 374, 335, and 250 cm^{-1} . Similar results were reported by other authors [49,50]. The calculated Raman spectrum of Li_2MnO_3 is shown in Figure 5d. Interestingly, the theoretical spectrum shows similar characteristics to the experimental one, showing minor differences in intensities. The results show eight Raman signals. Two main Raman active modes were evidenced at high and middle frequencies around 620 and 522 cm^{-1} . These bands can be assigned to A_g and B_g modes due to the vibrations of the Mn atoms and the vibrations of Li atoms in the Mn layer, respectively [50,51]. Two representative atomic displacements for the Raman vibration modes of Li_2MnO_3 are shown in Figure 6. Interestingly, our phonon and Raman simulations are in agreement.

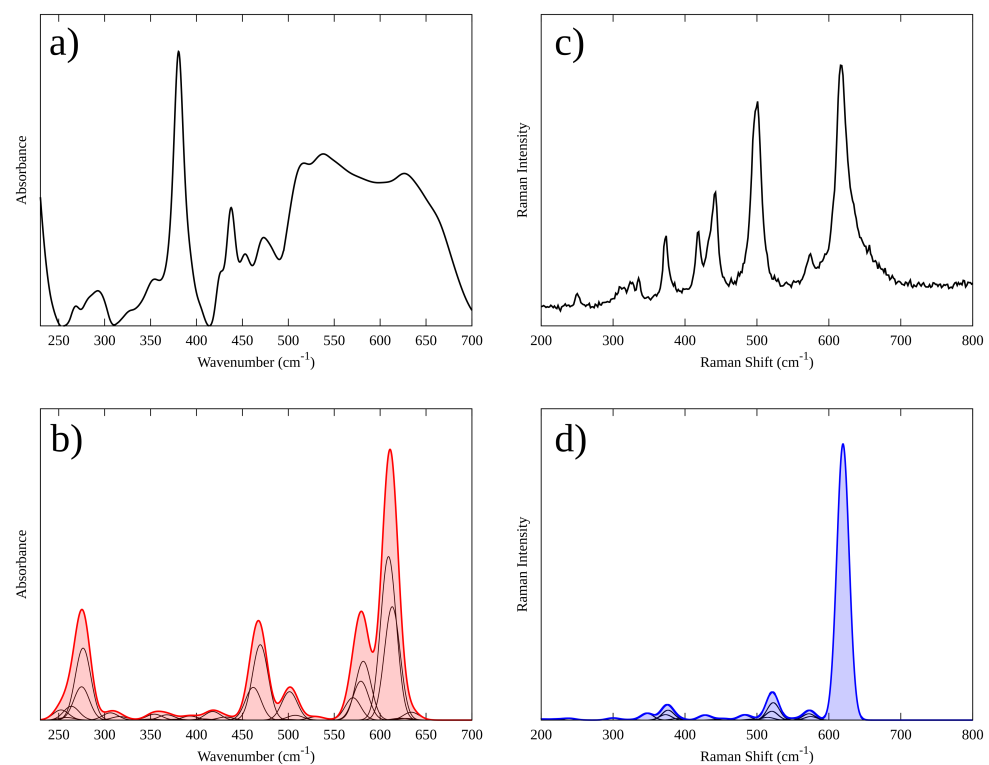


Figure 5. Experimental and theoretical IR (a,b) and Raman (c,d) spectra of Li_2MnO_3 .

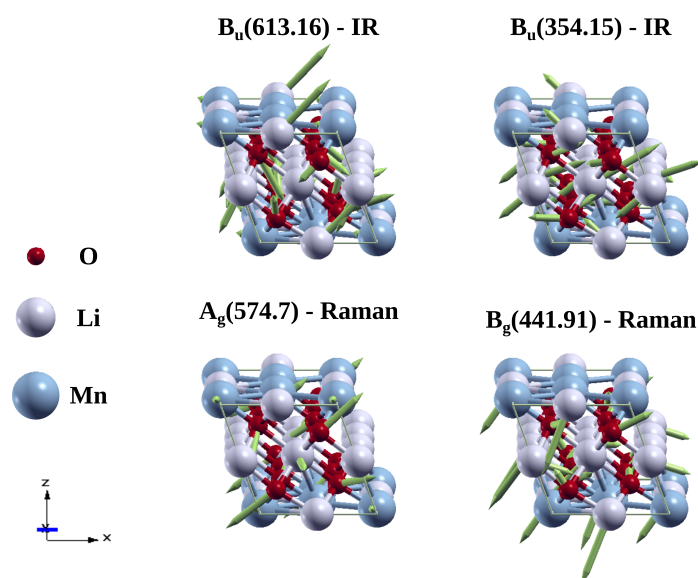


Figure 6. Atomic displacements for representatives IR and Raman vibrations modes of Li_2MnO_3 calculated by LDA.

4. Conclusions

In the present study, we have systematically computed the phonon structure, infrared, and Raman spectra of Li_2MnO_3 by first-principles calculations. We analyzed its crystal structure, optical phonon frequencies, IR, and Raman active mode and compared them to the experimental findings. By using the LDA exchange functional, we have found an underestimation of the lattice parameters by approximately 3% compared to the experimental one. Moreover, the electronic properties evidenced a semiconductor behavior with a strong hybridization between Mn $3d$ and O $2p$ states near the Fermi level. From the point of view of the vibrational properties, the phonon band structure of Li_2MnO_3 does not show a phonon gap. Additionally, the phonon distribution shows that Mn and O vibrational states dominate at higher frequencies, and Li and O atoms mainly contribute to the middle-to-low part of the spectrum. Simulated IR and Raman spectra agree with the experimental data. Thus, this work can be considered helpful for future studies dealing with the vibrational characterization of Li_2MnO_3 material.

Author Contributions: Conceptualization, R.P., N.N. and M.M.-S.; Experimental analysis, R.P., N.N., R.J.M.-P., G.R.-S., F.A.-R., I.B. and J.H.-M.; Theoretical calculations, R.P., N.N., R.J.M.-P., M.M.-S. and V.R.F.; writing—original draft preparation, R.P. and N.N. All authors have read and agreed to the published version of the manuscript.

Funding: This work was financially supported by CONICYT PFCHA/DOCTORADO/2015-21151648 (Ruth Pulido) and PFCHA/DOCTORADO/2017-21172001 (Nelson Naveas), and with partial funding for accessing research infrastructures granted by project PID2020-112770RB-C22, from the Ministerio de Ciencia e Innovación (Spain). The simulations used in this paper have been performed in the Centro de Computación Científica-Universidad Autónoma de Madrid (CCC-UAM); thanks to CPU time and other resources granted by the institution.

Institutional Review Board Statement: Not applicable.

Informed Consent Statement: Not applicable.

Data Availability Statement: The data that support the findings of this study are available from the corresponding author upon reasonable request.

Acknowledgments: We recognize PhD programs in “Advanced Materials and Nanotechnologies” from Universidad Autónoma de Madrid (UAM, Spain) and “Ingeniería de Procesos de Minerales” from Universidad de Antofagasta (UA, Chile).

Conflicts of Interest: The authors declare no conflict of interest. The funders had no role in the design of the study, in the collection, analysis, or interpretation of data, in the writing of the manuscript, or in the decision to publish the results.

Abbreviations

The following abbreviations are used in this manuscript:

DFT	Density Functional Theory
DFPT	Density Functional Perturbation Theory
LMO	Lithium Manganese Oxide
LDA	Local Density Approximation
DOS	Density of States
IR	Infrared

References

1. Karrech, A.; Azadi, M.A.; Elchalakani, M.; Shahin, M.A.; Seibi, A.C. A review on methods for liberating lithium from pegmatites. *Miner. Eng.* **2020**, *145*, 106085. [[CrossRef](#)]
2. Potapenko, A.V.; Kirillov, S.A. Lithium manganese spinel materials for high-rate electrochemical applications. *J. Energy Chem.* **2014**, *23*, 543–558. [[CrossRef](#)]
3. Pan, H.; Zhang, S.; Chen, J.; Gao, M.; Liu, Y.; Zhu, T.; Jiang, Y. Li- and Mn-rich layered oxide cathode materials for lithium-ion batteries: A review from fundamentals to research progress and applications. *Mol. Syst. Des. Eng.* **2018**, *3*, 748–803. [[CrossRef](#)]
4. Yu, H.; Naidu, G.; Zhang, C.; Wang, C.; Razmjou, A.; Han, D.S.; He, T.; Shon, H. Metal-based adsorbents for lithium recovery from aqueous resources. *Desalination* **2022**, *539*, 115951. [[CrossRef](#)]
5. Xu, X.; Chen, Y.; Wan, P.; Gasem, K.; Wang, K.; He, T.; Adidharma, H.; Fan, M. Extraction of lithium with functionalized lithium ion-sieves. *Prog. Mater. Sci.* **2016**, *84*, 276–313. [[CrossRef](#)]
6. Marincas, A.H.; Goga, F.; Dorneanu, S.; Ilea, P. Review on synthesis methods to obtain LiMn_2O_4 -based cathode materials for Li-ion batteries. *J. Solid State Electrochem.* **2020**, *24*, 473–497. [[CrossRef](#)]
7. Mabokela, T.; Nwanya, A.; Ndipingwi, M.; Kaba, S.; Ekwere, P.; Werry, S.; Ikpo, C.; Modibane, K.; Iwuoha, E. Review—Recent Advances on High-Capacity Li Ion-Rich Layered Manganese Oxide Cathodes. *J. Electrochem. Soc.* **2021**, *168*, 070530. [[CrossRef](#)]
8. Pulido, R.; Naveas, N.; Graber, T.; Martín-Palma, R.J.; Agulló-Rueda, F.; Brito, I.; Morales, C.; Soriano, L.; Pascual, L.; Marini, C.; et al. Hydrothermal control of the lithium-rich Li_2MnO_3 phase in lithium manganese oxide nanocomposites and their application as precursors for lithium adsorbents. *Dalton Trans.* **2021**, *50*, 10765–10778. [[CrossRef](#)]
9. Li, Y.; Makita, Y.; Lin, Z.; Lin, S.; Nagaoka, N.; Yang, X. Synthesis and characterization of lithium manganese oxides with core-shell $\text{Li}_4\text{Mn}_5\text{O}_{12}@\text{Li}_2\text{MnO}_3$ structure as lithium battery electrode materials. *Solid State Ionics* **2011**, *196*, 34–40. [[CrossRef](#)]
10. Johnson, C.; Li, N.; Vaughey, J.; Hackney, S.; Thackeray, M. Lithium–manganese oxide electrodes with layered–spinel composite structures $x\text{Li}_2\text{MnO}_3 \cdot (1-x)\text{Li}_{1+y}\text{Mn}_{2-y}\text{O}_4$ ($0 < x < 1$, $0 \leq y \leq 0.33$) for lithium batteries. *Electrochem. Commun.* **2005**, *7*, 528–536. [[CrossRef](#)]
11. Pulido, R.; Naveas, N.; Martín-Palma, R.J.; Graber, T.; Brito, I.; Hernández-Montelongo, J.; Manso Silván, M. Experimental and density functional theory study of the Li^+ desorption in spinel/layered lithium manganese oxide nanocomposites using HCl. *Chem. Eng. J.* **2022**, *441*, 136019. [[CrossRef](#)]
12. Song, Y.; Zhao, X.; Wang, C.; Bi, H.; Zhang, J.; Li, S.; Wang, M.; Che, R. Insight into the atomic structure of Li_2MnO_3 in Li-rich Mn-based cathode materials and the impact of its atomic arrangement on electrochemical performance. *J. Mater. Chem. A* **2017**, *5*, 11214–11223. [[CrossRef](#)]
13. Xiao, R.; Li, H.; Chen, L. Density Functional Investigation on Li_2MnO_3 . *Chem. Mater.* **2012**, *24*, 4242–4251. [[CrossRef](#)]
14. Thackeray, M.M.; Johnson, C.S.; Vaughey, J.T.; Li, N.; Hackney, S.A. Advances in manganese-oxide ‘composite’ electrodes for lithium-ion batteries. *J. Mater. Chem.* **2005**, *15*, 2257–2267. [[CrossRef](#)]
15. Zhu, Z.; Zhuo, S. Nano layered-spinel $0.8\text{Li}_2\text{MnO}_3 \cdot 0.2\text{LiMn}_2\text{O}_4$ as high-performance cathode for Li-ion batteries. *IOP Conf. Ser. Mater. Sci. Eng.* **2020**, *733*, 012005. [[CrossRef](#)]
16. Wei, Y.; Kim, K.B.; Chen, G. Evolution of the local structure and electrochemical properties of spinel $\text{LiNi}_x\text{Mn}_{2-x}\text{O}_4$ ($0 \leq x \leq 0.5$). *Electrochim. Acta* **2006**, *51*, 3365–3373. [[CrossRef](#)]
17. Zhao, W.; Xiong, L.; Xu, Y.; Xiao, X.; Wang, J.; Ren, Z. Magnesium substitution to improve the electrochemical performance of layered Li_2MnO_3 positive-electrode material. *J. Power Sources* **2016**, *330*, 37–44. [[CrossRef](#)]
18. Kim, K.W.; Lee, S.W.; Han, K.S.; Chung, H.J.; Woo, S.I. Characterization of Al-doped spinel LiMn_2O_4 thin film cathode electrodes prepared by Liquid Source Mist Chemical Deposition (LSMCD) technique. *Electrochim. Acta* **2003**, *48*, 4223–4231. [[CrossRef](#)]

19. Gao, A.; Hou, X.; Sun, Z.; Li, S.; Li, H.; Zhang, J. Lithium-desorption mechanism in LiMn_2O_4 , $\text{Li}_{1.33}\text{Mn}_{1.67}\text{O}_4$, and $\text{Li}_{1.6}\text{Mn}_{1.6}\text{O}_4$ according to precisely controlled acid treatment and density functional theory calculations. *J. Mater. Chem. A* **2019**, *7*, 20878–20890. [[CrossRef](#)]
20. Julien, C.M.; Massot, M. Lattice vibrations of materials for lithium rechargeable batteries III. Lithium manganese oxides. *Mater. Sci. Eng. B* **2003**, *100*, 69–78. [[CrossRef](#)]
21. Julien, C. Local Environment in 4-Volt Cathode Materials for Li-Ion Batteries. In *Materials for Lithium-Ion Batteries*; Julien, C., Stoynov, Z., Eds.; Springer: Dordrecht, The Netherlands, 2000; pp. 309–326. [[CrossRef](#)]
22. Julien, C.; Mauger, A. In situ Raman analyses of electrode materials for Li-ion batteries. *AIMS Mater. Sci.* **2018**, *5*, 650–698. [[CrossRef](#)]
23. Julien, C.; Massot, M. Structural Transitions in Positive Electrodes for Li-Ion Batteries the Vibronic Approach. *Ionics* **2002**, *8*, 6–16. [[CrossRef](#)]
24. Julien, C.M.; Massot, M. Raman spectroscopic studies of lithium manganates with spinel structure. *J. Phys. Condens. Matter* **2003**, *15*, 3151–3162. [[CrossRef](#)]
25. Julien, C.M. Local structure of lithiated manganese oxides. *Solid State Ionics* **2006**, *177*, 11–19. [[CrossRef](#)]
26. Julien, C.M.; Massot, M. Lattice vibrations of materials for lithium rechargeable batteries I. Lithium manganese oxide spinel. *Mater. Sci. Eng. B* **2003**, *97*, 217–230. [[CrossRef](#)]
27. Cheng, M.; Tang, W.; Sun, Y.; Zhu, K. Electrochemical properties of Li_2MnO_3 nanocrystals synthesized using a hydrothermal method. *RSC Adv.* **2015**, *5*, 71088–71094. [[CrossRef](#)]
28. Dheivamalar, S.; Silambarasan, V. DFT simulations and vibrational analysis of FTIR and FT-Raman spectra of 2-amino-4-methyl benzonitrile. *Spectrochim. Acta Part A Mol. Biomol. Spectrosc.* **2012**, *96*, 480–484. [[CrossRef](#)]
29. Ratnaparkhe, A.; Lambrecht, W.R.L. Calculated phonon modes, infrared, and Raman spectra in $\text{ZnGeGa}_2\text{N}_4$. *J. Appl. Phys.* **2020**, *128*, 075702. [[CrossRef](#)]
30. Oreshonkov, A.S.; Sukhanova, E.V.; Popov, Z.I. Raman Spectroscopy of Janus MoSSe Monolayer Polymorph Modifications Using Density Functional Theory. *Materials* **2022**, *15*, 3988. [[CrossRef](#)]
31. Giannozzi, P.; Baroni, S.; Bonini, N.; Calandra, M.; Car, R.; Cavazzoni, C.; Ceresoli, D.; Chiarotti, G.L.; Cococcioni, M.; Dabo, I.; et al. QUANTUM ESPRESSO: A modular and open-source software project for quantum simulations of materials. *J. Phys. Condens. Matter* **2009**, *21*, 395502. [[CrossRef](#)]
32. van Setten, M.; Giantomassi, M.; Bousquet, E.; Verstraete, M.; Hamann, D.; Gonze, X.; Rignanese, G.M. The PseudoDojo: Training and grading a 85 element optimized norm-conserving pseudopotential table. *Comput. Phys. Commun.* **2018**, *226*, 39–54. [[CrossRef](#)]
33. Monkhorst, H.J.; Pack, J.D. Special points for Brillouin-zone integrations. *Phys. Rev. B* **1976**, *13*, 5188–5192. [[CrossRef](#)]
34. Hoang, K. Defect Physics, Delithiation Mechanism, and Electronic and Ionic Conduction in Layered Lithium Manganese Oxide Cathode Materials. *Phys. Rev. Appl.* **2015**, *3*, 24013. [[CrossRef](#)]
35. Chen, H.; Islam, M.S. Lithium Extraction Mechanism in Li-Rich Li_2MnO_3 Involving Oxygen Hole Formation and Dimerization. *Chem. Mater.* **2016**, *28*, 6656–6663. [[CrossRef](#)]
36. Hoang, K. Doping Li-rich cathode material Li_2MnO_3 : Interplay between lattice site preference, electronic structure, and delithiation mechanism. *Phys. Rev. Mater.* **2017**, *1*, 075404. [[CrossRef](#)]
37. Giannozzi, P.; Andreussi, O.; Brumme, T.; Bunau, O.; Nardelli, M.B.; Calandra, M.; Car, R.; Cavazzoni, C.; Ceresoli, D.; Cococcioni, M.; et al. Advanced capabilities for materials modelling with Quantum ESPRESSO. *J. Phys. Condens. Matter* **2017**, *29*, 465901. [[CrossRef](#)]
38. Kokalj, A. Computer graphics and graphical user interfaces as tools in simulations of matter at the atomic scale. *Comput. Mater. Sci.* **2003**, *28*, 155–168. [[CrossRef](#)]
39. Nakao, Y.; Ozawa, K.; Nemoto, Y.; Uesugi, F.; Fujii, H.; Mochiku, T. Structural variation of Li_2MnO_3 during charge-discharge cycling. *Nippon. Seramikkusu Kyokai Gakujutsu Ronbunshij. Ceram. Soc. Jpn.* **2015**, *123*, 589–594. [[CrossRef](#)]
40. Shimoda, K.; Oishi, M.; Matsunaga, T.; Murakami, M.; Yamanaka, K.; Arai, H.; Ukyo, Y.; Uchimoto, Y.; Ohta, T.; Matsubara, E.; et al. Direct observation of layered-to-spinel phase transformation in Li_2MnO_3 and the spinel structure stabilised after the activation process. *J. Mater. Chem. A* **2017**, *5*, 6695–6707. [[CrossRef](#)]
41. Kaewmala, S.; Limphirat, W.; Yordsri, V.; Kim, H.; Muhammad, S.; Yoon, W.S.; Srilomsak, S.; Limthongkul, P.; Meethong, N. Structural and Electrochemical Kinetic Properties of $0.5\text{Li}_2\text{MnO}_3 \cdot 0.5\text{LiCoO}_2$ Cathode Materials with Different Li_2MnO_3 Domain Sizes. *Sci. Rep.* **2019**, *9*, 427. [[CrossRef](#)]
42. Boulineau, A.; Croguennec, L.; Delmas, C.; Weill, F. Structure of Li_2MnO_3 with different degrees of defects. *Solid State Ionics* **2010**, *180*, 1652–1659. [[CrossRef](#)]
43. Boulineau, A.; Croguennec, L.; Delmas, C.; Weill, F. Reinvestigation of Li_2MnO_3 Structure: Electron Diffraction and High Resolution TEM. *Chem. Mater.* **2009**, *21*, 4216–4222. [[CrossRef](#)]
44. Huang, Y.; Liu, L.; Gao, M. Molecular dynamics study on the Li diffusion mechanism and delithiation process of Li_2MnO_3 . *Solid State Ionics* **2020**, *346*, 115195. [[CrossRef](#)]
45. Zhang, X.; Zheng, F.; Wu, S.; Zhu, Z. Identifying a Li-rich superionic conductor from charge–discharge structural evolution study: Li_2MnO_3 . *Phys. Chem. Chem. Phys.* **2021**, *23*, 4829–4834. [[CrossRef](#)] [[PubMed](#)]

46. Saraiva, G.; da Silva Filho, J.; Saraiva-Souza, A.; de Castro, A.R.; Teixeira, A.; Luz-Lima, C.; Oliveira, F.; Neto, V.S.; Freire, P.; de Sousa, F. Temperature dependence Raman spectroscopy and DFT calculations of $\text{Bi}_2(\text{MoO}_4)_3$. *Spectrochim. Acta Part A Mol. Biomol. Spectrosc.* **2020**, *224*, 117340. [[CrossRef](#)]
47. Moura, J.; Silveira, J.; da Silva Filho, J.; Souza Filho, A.; Luz-Lima, C.; Freire, P. Temperature-induced phase transition in h-MoO₃: Stability loss mechanism uncovered by Raman spectroscopy and DFT calculations. *Vib. Spectrosc.* **2018**, *98*, 98–104. [[CrossRef](#)]
48. Post, J.; Mckeown, D.; Heaney, P. Raman spectroscopy study of manganese oxides: Tunnel structures. *Am. Mineral.* **2020**, *105*, 1175–1190. [[CrossRef](#)]
49. Yu, D.Y.W.; Yanagida, K. Structural Analysis of Li_2MnO_3 and Related Li-Mn-O Materials. *J. Electrochem. Soc.* **2011**, *158*, A1015. [[CrossRef](#)]
50. Ruther, R.E.; Dixit, H.; Pezeshki, A.M.; Sacci, R.L.; Cooper, V.R.; Nanda, J.; Veith, G.M. Correlating Local Structure with Electrochemical Activity in Li_2MnO_3 . *J. Phys. Chem. C* **2015**, *119*, 18022–18029. [[CrossRef](#)]
51. Torres-Castro, L.; Shojan, J.; Julien, C.M.; Huq, A.; Dhital, C.; Paranthaman, M.P.; Katiyar, R.S.; Manivannan, A. Synthesis, characterization and electrochemical performance of Al-substituted Li_2MnO_3 . *Mater. Sci. Eng. B* **2015**, *201*, 13–22. [[CrossRef](#)]